Theory of light emission in sonoluminescence as thermal radiation

Wang-Kong Tse* and P. T. Leung†
Physics Department and Institute of Theoretical Physics, The Chinese University of Hong Kong, Shatin, Hong Kong SAR, China
(Received 6 December 2005; published 3 May 2006)

Based on the model proposed by Hilgenfeldt *et al.* [Nature (London) **398**, 401 (1999)], we present here a comprehensive theory of thermal radiation in single-bubble sonoluminescence (SBSL). We first invoke the generalized Kirchhoff's law to obtain the thermal emissivity from the absorption cross section of a multilayered sphere (MLS). A sonoluminescing bubble, whose internal structure is determined from hydrodynamic simulations, is then modeled as a MLS and in turn the thermal radiation is evaluated. Numerical results obtained from simulations for argon bubbles show that our theory successfully captures the major features observed in SBSL experiments.

DOI: 10.1103/PhysRevE.73.056302 PACS number(s): 78.60.Mq, 42.25.Bs, 52.25.Os, 52.40.Db

I. INTRODUCTION

Single-bubble sonoluminescence (SBSL or simply SL), first discovered in 1989, is a phenomenon of periodic light emission by an oscillating gas bubble trapped in the pressure antinode of a standing ultrasound wave in water (or other fluids) (see [1,2] for detailed reviews on SBSL). The oscillating bubble is stable enough to survive many days through billions of acoustic cycles while the produced flashes are highly regular and incandescent. The width of the emitted light pulse is around 10–100 ps with a peak power of the order 10 mW [1–4]. The light pulse has nearly a Gaussian shape with a slight asymmetry, which is basically identical in the red and UV portions of the spectrum [4], and Hiller *et al.* [5] further confirmed that the pulse width and the emission time were independent of wavelength. However, in an interesting twist, Moran and Sweider [6] demonstrated that the pulse width did exhibit a mild dependence on wavelength at 3 °C, but not at 24 °C. Besides, the power spectrum of the emitted light was found to be broadband without any characteristic line, decreasing from the UV portion toward the red in a way that bore a resemblance to a blackbody spectrum [5,7,8].

SBSL has become an intriguing topic and an arena for experimentalists and theorists alike since its discovery. Numerous attempts have been made to study the bubble motion using classical bubble dynamics and sophisticated computational fluid mechanics (CFM) [9–16]. It is generally believed that the bubble is heated to temperatures of tens of thousands and shock waves and plasma could be generated during the contraction of the bubble. Various proposals have been put forward to explain the light emission mechanism, including surface blackbody radiation [1,7,17,18], neutral and ion bremsstrahlung [12,13,16,19–21], collision-induced emission [22,23], quantum vacuum radiation [24], confined-electron model [25], proton-tunneling [26], and nuclear fusion [27–29]. Some of these proposals, e.g., [1,7,12,13,16–23], attributed light emission in SBSL to the high temperature attained in the bubble and are classified as thermal radiation schemes in this paper. While qualitatively reproducing the spectra detected in SBSL, most of such thermal schemes failed to explain why the pulse width is wavelength independent as measured in some experiments [4,5]. Owing to this major drawback of thermal schemes, researchers were forced to look into other nonthermal and more exotic models (see, e.g., [24–29]).

To reconcile the success and the drawback of thermal radiation schemes, Hilgenfeldt, Grossmann, and Lohse [20,21] took the finite opacity of the bubble into consideration and obtained a wavelength-independent pulse width for argon bubbles. The impact of the Hilgenfeldt *et al.* work is huge and, to some extent, resurrects the thermal radiation scheme. However, it is worthwhile to note that the approach adopted in [20,21] is deemed a simplified version of the emission mechanism of SBSL as several physical processes have not been included in the proposal [30]. For example, the sonoluminescing bubble is modeled as a uniform one and the fluid dynamics inside the bubble has been neglected from the outset [20,21]. Besides, the Kirchhoff's law used in [20,21] to evaluate thermal emissivity of the bubble has completely ignored the wave nature of light.

In addition, existing literature (e.g., [2,31–33]) demonstrates there exists a gap in the theoretical treatment of light emission mechanism of sonoluminescence, in that blackbody radiation and thermal bremsstrahlung are often ascribed as separate possible mechanisms of SBSL. Often, Planck's formula for blackbody radiation [31,32] and absorption coefficients for thermal bremsstrahlung in vacuum [20,21] are applied separately in these cases, and the question of whether the bubble is opaque enough to demonstrate blackbody radiation is argued in a rather hand-waving manner by comparing the photon mean path with an estimated size of the light-emitting region. In our view, this is because of the lack of a single theory which can take account of both mechanisms in a finite-sized environment (i.e., the bubble) in a unifying manner. In a recent experimental paper [33], Flannigan and Suslick demonstrated conclusively the existence of a plasma state inside the bubble, and hence thermal bremsstrahlung is an inevitable consequence because of the motion

*Present address: Condensed Matter Theory Center, Department of Physics, University of Maryland at College Park, College Park, Maryland 20742-4111.
†Electronic address: ptleung@phy.cuhk.edu.hk

of the electrons and ions. We emphasize that blackbody radiation and thermal bremsstrahlung are nothing but one single emission mechanism manifested upon the degree of optical thickness of the bubble; and to this purpose, in this paper we have developed a coherent theory unifying both aspects in the context of SBSL. Within the framework of this theory, when the bubble becomes optically thick enough, the thermal bremsstrahlung manifest itself asymptotically as blackbody radiation.

First, we will consider thermal emission in a realistic sonoluminescing bubble that is nonuniform in temperature as well as density. To properly describe processes of thermal emission and absorption in a finite volume with a size comparable to the wavelength of light in a consistent manner, the generalized Kirchhoff's law is used in our paper [34]. Second, state-of-the-art CFM is applied here to evaluate the temperature and density distributions in the bubble [14,15]. Through such elaboration of the thermal radiation scheme [20,21], we succeed in obtaining an emission spectrum that agrees nicely with the experimental data as summarized in [1] and, in addition, resolve the dilemma of whether the pulse width is dependent on the wavelength.

The rest of this paper is organized as follows. We first present the generalized Kirchhoff's law in Sec. II, and show in Sec. III that it leads to the formula for emissivity used in [20,21] in certain limits. In Secs. IV and V we make use of the generalized Kirchhoff's law to derive the spectral radiance of a heated multilayered sphere. In Secs. VI and VII, respectively, we furnish the plasma model and CFM used in the present paper. We then present relevant numerical results in Sec. VIII and conclude our paper in Sec. IX.

II. THERMAL RADIATION

In SL, the high temperature reached inside the bubble ionizes the gas content, forming a partially ionized plasma [16,20,21,35,36]. Besides having finite optical thickness, the bubble has a size $\sim 0.1-1$ μm near the instant of maximum compression, which is comparable to the wavelength of the emitted light ranging from 200 to 800 nm. Hence, the assumption of geometric optics is invalid. To properly take account of the effects of finite absorption, wave reflection, and diffraction, we employ in this paper the generalized Kirchhoff's law [34], which yields the "classical" form of Kirchhoff's law as an asymptotic limit, to compute the power spectrum.

We first review the statement of the "classical" form of Kirchhoff's law (see, e.g., [37]). Consider an isotropic absorbing medium with complex dielectric constant $\epsilon=\epsilon_R+i\epsilon_I$, refractive index $n=\sqrt{\epsilon}=n_R+in_I$, and a typical size d. If the medium is in thermal equilibrium at temperature T and d is large compared with the wavelength of light λ so that the geometric optics approximation holds, then the classical form of Kirchhoff's law relates the emission coefficient $\eta(\omega)$ and the absorption coefficient $\kappa(\omega)\equiv 2n_I\omega/c$ at (angular) frequency $\omega\equiv 2\pi f$ as [37]

$$\eta/\kappa = n_R^2 B_\omega(T), \tag{2.1}$$

where

$$B_\omega(T) = \frac{\hbar\omega^3}{8\pi^3 c^2 (e^{\hbar\omega/k_B T}-1)} \tag{2.2}$$

is the (frequency) spectral light intensity of a blackbody for one polarization, with c, $\hbar$, and k_B being the speed of light in vacuum, the Planck constant h divided by 2π, and the Boltzmann constant, respectively. We remark that, besides the assumption $\lambda \ll d$, its application is justified only to a volume emitter which is optically thin.

The generalized Kirchhoff's law [34] is a generalization of the classical form of Kirchhoff's law to all sizes d and optical thickness of a finite-size emitter, and can be derived from the Maxwell equations

$$\boldsymbol{\nabla}\cdot\boldsymbol{D}(\boldsymbol{r},t) = \rho_n(\boldsymbol{r},t), \tag{2.3}$$

$$\boldsymbol{\nabla}\cdot\boldsymbol{B}(\boldsymbol{r},t) = 0, \tag{2.4}$$

$$\boldsymbol{\nabla}\times\boldsymbol{E}(\boldsymbol{r},t) + \frac{\partial\boldsymbol{B}(\boldsymbol{r},t)}{\partial t} = \boldsymbol{0}, \tag{2.5}$$

$$\boldsymbol{\nabla}\times\boldsymbol{H}(\boldsymbol{r},t) - \frac{\partial\boldsymbol{D}(\boldsymbol{r},t)}{\partial t} = \boldsymbol{J}_n(\boldsymbol{r},t). \tag{2.6}$$

Here the electric field $\boldsymbol{E}$, the magnetic induction $\boldsymbol{B}$, the displacement field $\boldsymbol{D}$, and the magnetic field strength $\boldsymbol{H}$ are generated by the fluctuating charge density ρ_n and current density $\boldsymbol{J}_n$, which are a direct consequence of the random thermal motions of the charges and satisfy the fluctuation-dissipation theorem (see, e.g., [38])

$$\langle \tilde{J}_{n,i}(\boldsymbol{r},\omega)\tilde{J}^*_{n,j}(\boldsymbol{r}',\omega)\rangle = \frac{4\omega}{\pi}\theta(\omega,T)\epsilon_0\epsilon_I(\boldsymbol{r},\omega)\delta(\boldsymbol{r}-\boldsymbol{r}')\delta_{ij}. \tag{2.7}$$

Here $\tilde{J}_{n,i}(\boldsymbol{r},\omega)$ is the i component of the Fourier transform of $\boldsymbol{J}_n(\boldsymbol{r},t)$,

$$\theta(\omega,T) = \frac{\hbar\omega}{2}\coth\frac{\hbar\omega}{2k_B T} \tag{2.8}$$

is the average energy of a quantum harmonic oscillator at temperature T, and ϵ_0 is permittivity constant of vacuum.

In the presence of the thermal fluctuations ρ_n and $\boldsymbol{J}_n$, all fields $\boldsymbol{E}$, $\boldsymbol{D}$, $\boldsymbol{H}$, and $\boldsymbol{B}$ are thermally fluctuating quantities. The set of stochastic Eqs. (2.3)–(2.6), together with the fluctuation-dissipation theorem, completely determine the statistics of the electromagnetic field of such a system and the relevant theory is termed the thermal electromagnetic theory (TET) [34].

The generalized Kirchhoff's law derived from TET [34] states that the spectral radiance P_λ, defined as the power emitted per unit wavelength interval and unit solid angle, is given by the following formula [34]:

$$P_\lambda(\mathbf{n}) = B_\lambda(T)\sigma_{\mathrm{abs}}(\mathbf{n}). \tag{2.9}$$

Here $P_\lambda(\mathbf{n})$ is the spectral radiance in the direction of $\mathbf{n}\equiv\mathbf{r}/|\mathbf{r}|$, $\sigma_{\mathrm{abs}}(\mathbf{n})$ is the absorption cross-sectional area of the emitter for an electromagnetic wave illuminating the emitter from the direction of $\mathbf{n}$, and

$$B_\lambda(T) = \frac{hc^2}{\lambda^5(e^{hc/\lambda k_B T} - 1)} \tag{2.10}$$

is the spectral light intensity in each polarization for an ideal blackbody. In Eq. (2.9) it is understood that σ_{abs} is the sum of the absorption cross-sectional areas for incident light waves with two perpendicular polarizations. It is evident that σ_{abs} is equal to the power P_a dissipated in the emitter for an incident plane wave carrying unit energy flux, which can be obtained from the following volume integral over the emitter:

$$P_a = \frac{\omega}{2}\int d^3r \epsilon_0 \epsilon_I(\boldsymbol{r},\omega)|\boldsymbol{E}(\boldsymbol{r},\omega)|^2. \tag{2.11}$$

It is worthwhile to note that $\boldsymbol{E}(\boldsymbol{r},\omega)$ the electric field developed inside the emitter might be strongly enhanced at certain frequencies due to resonance effects and thus carries nontrivial frequency dependence [36].

Besides the spectral radiance, the integrated power of the emitted light pulse is another quantity measured in SBSL experiments and is simply the integral of Eq. (2.9) over the wavelength

$$P = \int_{\lambda_1}^{\lambda_2} d\lambda P_\lambda. \tag{2.12}$$

III. GEOMETRIC OPTICS MODEL

We now apply the generalized Kirchhoff's law summarized above to consider light emission in the uniform bubble model (UBM) as proposed in [20,21]. We will see that the formula for the spectral radiance used in [20,21] is only an approximate one that is valid only under certain restrictions.

To use a simple situation to elucidate the generalized Kirchhoff's law, we first calculate the power emitted from a slab. Consider a weakly absorbing slab illuminated normally by a plane-polarized plane wave with unit flux. Under the assumption that the slab (with thickness L and area A) has dimensions sufficiently large so that multiple internal reflections can be neglected and the internal electric field can be represented by a single decaying, traveling wave only, the internal power loss can be found from Eq. (2.11)

$$P_a = \frac{\omega\epsilon_0\epsilon_I}{\kappa c}(1 - p_{ref})A(1 - e^{-\kappa L}). \tag{3.1}$$

Here p_{ref} is the fraction of power reflected from the slab surface. For small absorption, the imaginary part of the refractive index $n_I \simeq \epsilon_I/2$, so

$$P_\lambda = 2(1 - p_{ref})B_\lambda(T)(1 - e^{-\kappa L})A, \tag{3.2}$$

where the factor of 2 properly takes care of the two possible polarizations. This result is consistent with that obtained from the standard radiative transfer theory [37,39], upon which the spectral radiance obtained in [20,21] is founded.

In the following we explicitly derive the formula for the spectral radiance that was used by Hilgenfeldt *et al.* in [20,21] from Eq. (3.2). Figure 1 shows a uniform sphere of radius R, which is divided into multiple thin cylindrical shells. Each of these shells, indicated by the dashed lines, subtends an angle of $\pi - 2\theta$ at the center, and has a length $L(\theta) = 2R\cos\theta$ along the x direction and a differential cross-sectional area $dA = 2\pi R^2 \sin\theta\cos\theta d\theta$. With the assumptions that (i) $p_{ref} = 0$, (ii) effects of refraction and diffraction at the spherical interface are negligible, (iii) internal reflection is ignorable, and (iv) each of these shells can be considered as a slab with area dA and thickness $L(\theta)$, the radiance per unit solid angle follows directly from Eq. (3.2) is given by

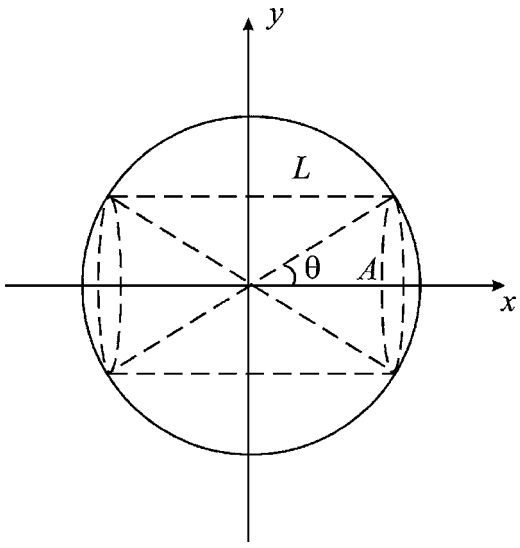

FIG. 1. The configuration of a uniform absorbing sphere.

$$P_\lambda = \int dA 2B_\lambda(T)(1 - e^{-\kappa z}) = 2\pi R^2 B_\lambda(T)\left[1 + \frac{e^{-2\kappa R}}{\kappa R} + \frac{e^{-2\kappa R} - 1}{2\kappa^2 R^2}\right]. \tag{3.3}$$

Multiplying this by the total solid angle 4π straightforwardly yields the formula Eq. (17) in Ref. [20]. As seen from the derivation here, this formula is only valid under the assumptions mentioned above, through which the wave nature of light has been completely neglected. Such an emission model will be referred to as the geometric optics model (GOM) in the following discussion. As we will show in our numerical results (Sec. VIII), the conditions for the validity of GOM do not generally hold in a realistic SL model.

IV. MULTILAYERED SPHERE

As discussed in Sec. III, Hilgenfeldt *et al.* [20,21] have assumed UBM as well as GOM in deriving the spectral radiance. This simplification serves as an illustration of the essential ingredients in SBSL. Yet its validity has to be verified, and for realistic calculations comparable to the experiment, it is necessary to take full account of the hydrodynamics inside the bubble. In light of this, in the following we will employ CFM developed by Ho *et al.* [35] to simulate the hydrodynamics of the bubble. It is then obvious that UBM breaks down in such a situation and, instead, we can model the inhomogeneous SL bubble as a multilayered sphere

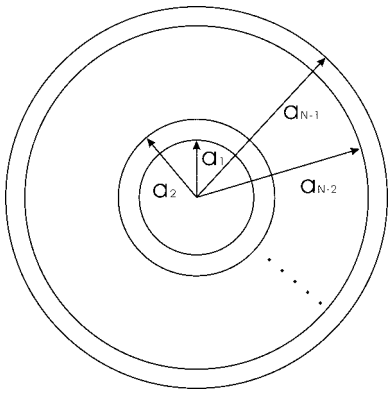

FIG. 2. A N-layered spherical system. The inner $N-1$ layers (the bubble) are absorbing, while the outermost layer (the surrounding fluid) is transparent.

(MLS) with a piecewise-constant configuration of temperature and refractive index (see Fig. 2). In realistic calculations, the number of layers is so large that MLS is able to mimic the continuous distribution obtained from CFM. On the other hand, MLS also includes UBM as a special case where there is only a single layer.

Consider a MLS (i.e., the bubble) having a piecewise-constant temperature profile $T=T_j$, $j=1,2,\ldots,N-1$. As the absorption cross section simply becomes the sum of the contribution from each layer, it follows directly from Eq. (2.9) that

$$P_\lambda = \sum_{j=1}^{N-1} B_\lambda(T_j)\sigma_{\mathrm{abs},j}, \tag{4.1}$$

where $\sigma_{\mathrm{abs},j}$ is the contribution of the jth layer to the total absorption cross section of the MLS. Equations (3.3) and (4.1) are the equations that we use for computing the power emitted from the SL bubble. In Sec. V we will evaluate $\sigma_{\mathrm{abs},j}$ from a wave optics perspective.

V. WAVE OPTICS MODEL

To evaluate $\sigma_{\mathrm{abs},j}$ in a MLS, we first determine the electromagnetic field inside the absorbing sphere using the transfer matrix formalism applicable to multilayered configuration (see, e.g., [36]).

Consider a circularly polarized plane wave illuminating an absorbing MLS (see Fig. 2). The MLS is composed of $N-1$ spherical shells, and the refractive index, the inner and outer radii of the jth shell ($j=1,2,\ldots,N-1$) are n_j, a_{j-1}, and a_j, respectively ($a_0=0$ and $a_{N-1}=R$ are assumed). The extended medium surrounding the MLS (i.e., the bubble) is considered as the Nth layer and has a refractive index n_N.

The electric and magnetic fields of the incident wave are given by $\boldsymbol{E}_{\mathrm{inc}}(\boldsymbol{r})=(\hat{\boldsymbol{x}}+i\hat{\boldsymbol{y}})\exp(ikz)$ and $\boldsymbol{B}_{\mathrm{inc}}(\boldsymbol{r})=-i\boldsymbol{E}(\boldsymbol{r})/c$.

Hereafter we assume that the wave has positive helicity. The electric and magnetic field inside the jth layer of the MLS ($j=1,2,\ldots,N$), can be, respectively, expressed in multipole expansion as

$$\boldsymbol{E}_j(\boldsymbol{r}) = \sum_{l=1}^{\infty} i^l\sqrt{4\pi(2l+1)} \times\left\{f_j^{(\mathrm{E})}\boldsymbol{Y}_{l,1}^{(0)} + \frac{\boldsymbol{\nabla}\times[f_j^{(\mathrm{M})}\boldsymbol{Y}_{l,1}^{(0)}]}{n_j k}\right\}, \tag{5.1}$$

$$\boldsymbol{B}_j(\boldsymbol{r}) = -\frac{in_j}{c}\sum_{l=1}^{\infty} i^l\sqrt{4\pi(2l+1)} \times\left\{f_j^{(\mathrm{M})}\boldsymbol{Y}_{l,1}^{(0)} + \frac{\boldsymbol{\nabla}\times[f_j^{(\mathrm{E})}\boldsymbol{Y}_{l,1}^{(0)}]}{n_j k}\right\}, \tag{5.2}$$

where the vector spherical harmonics $\boldsymbol{Y}_{lm}^{(0)}(\theta,\phi)\equiv -i\boldsymbol{r}\times\boldsymbol{\nabla}Y_{lm}(\theta,\phi)/\sqrt{l(l+1)}$, with $Y_{lm}(\theta,\phi)$ being the ordinary spherical harmonics [40].

For the extended medium where $j=N$, $f_N^{(\mathrm{E})}=f_N^{(\mathrm{M})}=j_l(n_N x)$, with j_l being the spherical Bessel function of the lth order and $x=kr$, Eqs. (5.1) and (5.2) reduce to the ordinary multipole expansion of a plane wave. For $j<N$, $f_j^{(\mu)}(r)$ ($\mu=\mathrm{E},\mathrm{M}$) are governed by the radial wave equation:

$$\left[\frac{\mathrm{d}^2}{\mathrm{d}r^2} + n_j^2k^2 - \frac{l(l+1)}{r^2}\right] r f_j^{(\mu)}(r) = 0, \tag{5.3}$$

and, in addition, they satisfy the standard boundary conditions on electromagnetic fields imposed at $r=a_j$

$$f_j^{(\mathrm{E})}(r) = f_{j+1}^{(\mathrm{E})}(r), \tag{5.4}$$

$$\frac{\mathrm{d}}{\mathrm{d}r}[rf_j^{(\mathrm{E})}] = \frac{\mathrm{d}}{\mathrm{d}r}[rf_{j+1}^{(\mathrm{E})}(r)], \tag{5.5}$$

$$n_j f_j^{(\mathrm{M})}(r) = n_{j+1} f_{j+1}^{(\mathrm{M})}(r), \tag{5.6}$$

$$\frac{n_{j+1}}{n_j}\frac{\mathrm{d}}{\mathrm{d}r}[rf_j^{(\mathrm{M})}] = \frac{\mathrm{d}}{\mathrm{d}r}[rf_{j+1}^{(\mathrm{M})}(r)]. \tag{5.7}$$

In general $f_j^{(\mu)}(r)$ can be written as

$$f_j^{(\mu)}(r) = \alpha_j^{(\mu)} j_l(n_j kr) + \beta_j^{(\mu)} h_l^{(1)}(n_j kr), \tag{5.8}$$

where $h_l^{(1)}$ is the lth order spherical Hankel function of the first kind. Substituting Eq. (5.8) into Eqs. (5.4)–(5.7) and recasting them into matrix form, we can show that

$$\begin{bmatrix}\alpha_{j+1}^{(\mu)}\\ \beta_{j+1}^{(\mu)}\end{bmatrix} = \mathbf{T}_j^{(\mu)}\begin{bmatrix}\alpha_j^{(\mu)}\\ \beta_j^{(\mu)}\end{bmatrix}, \tag{5.9}$$

where $\mathbf{T}_j^{(\mathrm{E})}$ and $\mathbf{T}_j^{(\mathrm{M})}$ are, respectively, the TE-mode and TM-mode transfer matrix at $r=a_j$, given explicitly by

$$\mathbf{T}_j^{(\mathrm{E})} = -in_{j+1}x_j^2 \times \begin{bmatrix} W_{j+1,j}^{(\mathrm{E})}[j_l(n_jx_j), h_l^{(1)}(n_{j+1}x_j)] & W_{j+1,j}^{(\mathrm{E})}[h_l^{(1)}(n_jx_j), h_l^{(1)}(n_{j+1}x_j)] \\ -W_{j+1,j}^{(\mathrm{E})}[j_l(n_jx_j), j_l(n_{j+1}x_j)] & -W_{j+1,j}^{(\mathrm{E})}[h_l^{(1)}(n_jx_j), j_l(n_{j+1}x_j)] \end{bmatrix}, \tag{5.10}$$

$$\mathbf{T}_j^{(\mathrm{M})} = -in_{j+1}^2 n_j x_j^2 \times \begin{bmatrix} W_{j+1,j}^{(\mathrm{M})}[j_l(n_jx_j), h_l^{(1)}(n_{j+1}x_j)] & W_{j+1,j}^{(\mathrm{M})}[h_l^{(1)}(n_jx_j), h_l^{(1)}(n_{j+1}x_j)] \\ -W_{j+1,j}^{(\mathrm{M})}[j_l(n_jx_j), j_l(n_{j+1}x_j)] & -W_{j+1,j}^{(\mathrm{M})}[h_l^{(1)}(n_jx_j), j_l(n_{j+1}x_j)] \end{bmatrix}. \tag{5.11}$$

Here $x_j = ka_j$, and for convenience we define the generalized Wronskian $W_{j+1,j}^{(\mu)}[f,g]$ for TE and TM modes as

$$W_{j+1,j}^{(\mathrm{E})}[f,g] = fg' - f'g, \tag{5.12}$$

$$W_{j+1,j}^{(\mathrm{M})}[f,g] = \frac{fg'}{n_{j+1}^2} - \frac{f'g}{n_j^2} + \left(\frac{1}{n_{j+1}^2} - \frac{1}{n_j^2}\right)\frac{fg}{x}, \tag{5.13}$$

where $' = \mathrm{d}/\mathrm{d}x$.

In short, the transfer matrix $\mathbf{T}_j^{(\mu)}$ can be written as

$$\mathbf{T}_j^{(\mu)} = \begin{bmatrix} A_j^{(\mu)} & B_j^{(\mu)} \\ C_j^{(\mu)} & D_j^{(\mu)} \end{bmatrix}. \tag{5.14}$$

We can now solve for the field coefficients $\alpha_j^{(\mu)}$ and $\beta_j^{(\mu)}$using the regularity condition at $r=0$ and radiation boundary conditions at $r=\infty$, leading to the following relation:

$$\begin{bmatrix} 1 \\ \beta_N^{(\mu)} \end{bmatrix} = \begin{bmatrix} A^{(\mu)} & B^{(\mu)} \\ C^{(\mu)} & D^{(\mu)} \end{bmatrix} \begin{bmatrix} \alpha_1^{(\mu)} \\ 0 \end{bmatrix}. \tag{5.15}$$

Here $A^{(\mu)}, B^{(\mu)}, C^{(\mu)}, D^{(\mu)}$ (without the subscript j) are the elements of the *total* transfer matrix $\mathbf{T}^{(\mu)}$ from the layer $j=1$ to the layer $j=N-1$, i.e., $\mathbf{T}^{(\mu)} = \mathbf{T}_{N-1}^{(\mu)}\mathbf{T}_{N-2}^{(\mu)}\cdots\mathbf{T}_1^{(\mu)}$. From Eq. (5.15) we immediately get

$$\alpha_1^{(\mu)} = (A^{(\mu)})^{-1}, \tag{5.16}$$

$$\beta_N^{(\mu)} = C^{(\mu)}\alpha_1^{(\mu)} = C^{(\mu)}/A^{(\mu)}. \tag{5.17}$$

The field coefficients of each layer $\alpha_j^{(\mu)}$, $\beta_j^{(\mu)}$ is now readily obtained by iteratively applying Eq. (5.9), from $j=1$ to $j=N-1$, using the boundary conditions Eqs. (5.16) and (5.17).

Now we proceed to calculate the absorption cross section of the jth spherical shell. To this end, we first evaluate

$$\mathcal{F}_j = \frac{n_N c a_j^2}{2}\mathrm{Re}\left\{\int \mathrm{d}\Omega \boldsymbol{E}_j(\hat{\boldsymbol{r}} \times \boldsymbol{B}_j^*)\right\}, \tag{5.18}$$

which is directly proportional to the energy flux $\mathcal{F}_j$ crossing the jth interface at $r=a_j$. With Eqs. (5.1) and (5.2), we find, after some algebraic manipulations

$$\mathcal{F}_j = \frac{2\pi x n_N}{k^2}\mathrm{Im}\left\{ n_j^* \sum_{l=1}^{\infty}(2l+1) \times \left[\frac{f_j^{(E)}[xf_j^{(E)}]'^*}{n_j^*} - \frac{f_j^{(M)*}[xf_j^{(M)}]'}{n_j}\right]\right\}, \tag{5.19}$$

where x is evaluated at $r=a_j$. Following directly from energy conservation, the absorption cross section of the jth spherical shell $\sigma_{\mathrm{abs},j}$ is given by the difference between $\mathcal{F}_j$ and $\mathcal{F}_{j-1}$

$$\sigma_{\mathrm{abs},j} = \mathcal{F}_j - \mathcal{F}_{j-1}. \tag{5.20}$$

Eqs. (5.19) and (5.20) in conjunction with Eqs. (2.12) and (4.1), with no simplifying assumptions based on geometric optics and optical thickness, are the major results of the wave optics model (WOM) introduced here, which will be used in this paper to calculate the light emission of a SL bubble.

VI. PLASMA MODEL OF MULTILAYERED SPHERE

A. Formation of Plasma

In order to consider light emission processes in a MLS, we have to find the complex refractive index n_j and hence the absorption coefficient κ_j of each layer. In the presence of the high temperature developed during the collapse of a SL bubble, the gas inside the bubble is partially ionized at the instant of light emission [13,19–21,35,36]. Here we adopt a simple collision-dominated plasma model in which the collision frequency ν is a constant dependent on the concentration and temperature of the plasma [37]. The refractive index is then given by

$$n^2(\omega) = n_b^2 - \frac{\omega_p^2}{\omega^2 + i\nu\omega}, \tag{6.1}$$

where $\omega_p = \sqrt{N_e e^2/m\epsilon_0}$ is the plasma frequency,

$$n_b = \left(\frac{1 + 2N_0\alpha/3\epsilon_0}{1 - N_0\alpha/3\epsilon_0}\right)^{1/2}, \tag{6.2}$$

is the contribution to the refractive index due to the background neutral atoms as given by the Clausius-Mossotti equation (see, e.g., [41]), and α is the atomic polarizability, with e and m being the charge and the mass of electron, respectively. For convenience we have suppressed the j dependence of the relevant physical quantities in the above equations. In the subsequent discussion we will use CFM

developed in [35] to determine the number densities of electron and atom N_e and N_0 as a function of time.

B. Collision Processes in plasma

Around the instant of maximum compression, the temperature of a sonoluminescing bubble could reach tens of thousands of kelvins, ionizing the gas content inside. While Ref. [20] showed that the fraction of Ar^+ ions amounts to less than 1% of the bubble content using a uniform bubble assumption, Ref. [35] took account of full hydrodynamics and showed that this fraction can be as large as 30%. However, both papers point to the fact that the bubble content becomes a partially ionized plasma with Ar being the dominant species. Under this condition, bremsstrahlung is thought to play a major role in the light emission mechanism; in particular, electron-atom bremsstrahlung is expected to be the dominant process compared to other bremsstrahlung processes [20,21].

On the other hand, as the numerical results obtained from CFM showed the degree of ionization may be much higher than those from UBM, we have developed here the WOM to take account of effects due to reflection, refraction, and diffraction as well. In accordance with the approach of WOM, one has to consider the total effective collision frequency ν, which is the sum of contributions from electron-ion collision, electron-atom collision, and electron-ion recombination. According to the initial and final states of the electron, the first two are also known as free-free transitions, the latter one as free-bound transition. Of course, the direct product of such collisions is the emission of photons and the corresponding mechanisms are electron-ion bremsstrahlung, electron-atom bremsstrahlung, as well as electron-ion recombination. Therefore, one can easily see the difference, as well as the relation between our approach and that proposed in [20,21]. In the following we provide the formulas of the collision frequencies in these processes.

1. Electron-ion collision

The simplest picture describing electron-ion collisions and electron-ion bremsstrahlung is to regard them as individual binary events so that collective phenomena do not enter. Under such an assumption the differential emission cross-section $d\sigma_f$, which measures the probability of light emission due to the scattering of a unit incident electron flux from an ion with charge Ze, is given by the well-known Kramer's formula [39]. It is customary to include quantum mechanical corrections to this classical formula as the Gaunt factor [37]. For free-free transitions, including the free-free Gaunt factor $g_{\mathrm{ff}}(f,v)$ gives $d\sigma_f$ as

$$\frac{\mathrm{d}\sigma_f}{\mathrm{d}f} = \left(\frac{e^2}{4\pi\epsilon_0 \hbar\, c}\right)^3 \frac{16\pi\hbar^2}{3\sqrt{3}m^2v^2}\frac{Z^2}{f} g_{\mathrm{ff}}(f,v), \tag{6.3}$$

where f is the light frequency and v is the speed of the incident electron. Within the range of optical frequencies, the free-free Gaunt factor is usually of the order 1.

The collisions between charged particles is formally described by the scattering cross-section $\sigma(\theta)$, measuring the probability of scattering at an angle θ of a unit incident electron flux from an ion. However, the cross section used in transport theory to predict the scattering frequency is σ_{tr}, related to the former through the relation $\sigma_{\mathrm{tr}}=\overline{\sigma(\theta)(1-\cos\theta)}$, where the overbar indicates averaging over the scattering angle θ. Using the relation between the differential emission cross-section $\mathrm{d}\sigma_f$ and the transport cross-section σ_{tr} [39]

$$\frac{\mathrm{d}\sigma_f}{\mathrm{d}f} = \frac{8}{3}\frac{e^2v^2}{4\pi\epsilon_0 c^3 hf}\sigma_{\mathrm{tr}}, \tag{6.4}$$

the transport cross section is found to be

$$\sigma_{\mathrm{tr}} = \frac{4\pi^2}{\sqrt{3}}\left(\frac{Ze^2}{4\pi\epsilon_0 mv^2}\right)^2 g_{\mathrm{ff}}(f,v). \tag{6.5}$$

The collision frequency, defined as $\nu=Nv\sigma_{\mathrm{tr}}$, where N is the number density of the background species (N_i for ions or N_0 for atoms), is then

$$\nu_{\mathrm{ei}} = \frac{4\pi^2}{\sqrt{3}}\frac{N_i Z^2 e^4}{(4\pi\epsilon_0)^2 m^2 v^3} g_{\mathrm{ff}}(f,v). \tag{6.6}$$

2. Electron-ion Recombination

In electron-ion recombination, an electron is first captured by an ion, forming a bound state with energy levels labeled by quantum number n. A photon is released in such a process and the differential emission cross section is given by Eq. (6.3) with the free-free Gaunt factor replaced by the free-bound Gaunt factor $g_{\mathrm{fb}}(n,f,v)$. In addition to its dependence on the photon frequency f and the velocity v of the incident electron, the free-bound Gaunt factor is also a function of n and approximately of the order unity in optical frequencies. Accordingly, the transport cross section and the electron-ion recombination collision frequency are given, respectively, by Eqs. (6.5) and (6.6) with $g_{\mathrm{fb}}(n,f,v)$ replacing $g_{\mathrm{ff}}(f,v)$.

3. Electron-atom collision

An electron moving near a neutral atom can also experience a short-range Coulomb field, emitting radiation commonly known as electron-atom bremsstrahlung. There is no simple theory to determine the corresponding transport cross section as we are aware of; and common practice is to determine it from experiment with different incident electron energies. With good accuracy in the relevant range of electron energies for an argon SL bubble, σ_{tr} has a linear dependence on the electron energy $E_e=mv^2/2$ and $\sigma_{\mathrm{tr}}=c_{\mathrm{tr}}mv^2/2+d_{\mathrm{tr}}$, with the empirical constants $c_{\mathrm{tr}}\simeq 0.1\ \mathrm{m^2\,J^{-1}}$ and $d_{\mathrm{tr}}\simeq -0.6\times 10^{-20}\ \mathrm{m^2}$ [20,42]. The electron-atom collision frequency is therefore

$$\nu_{\mathrm{ea}} = N_0 v(c_{\mathrm{tr}}mv^2/2 + d_{\mathrm{tr}}). \tag{6.7}$$

C. Effective collision frequency

Assuming local thermodynamic equilibrium prevails in the plasma (as in the case for SL) and weak damping ($\nu \ll \omega$), we proceed to calculate the effective collision fre-

quency [37] defined by $\nu^{\text{eff}}=\bar{\nu}=N\overline{v\sigma_{\text{tr}}(v)}$, here $\overline{\cdots}$ indicates the Maxwellian average

$$\overline{\cdots}=\frac{4\pi}{3}\left(\frac{m}{2\pi k_BT}\right)^{3/2}\left(\frac{m}{k_BT}\right)\int_0^\infty dv v^4 e^{-mv^2/2k_BT}(\cdots). \tag{6.8}$$

Accordingly, the effective collision frequencies for electron-ion bremsstrahlung, electron-ion recombination, and electron-atom bremsstrahlung are obtained as (for clarity we drop the superscript "eff"):

$$\nu_{\text{ei(rc)}}=2\left(\frac{2\pi}{3}\right)^{3/2}N_i\left(\frac{Ze^2}{4\pi\epsilon_0 k_BT}\right)^2\left(\frac{k_BT}{m}\right)^{1/2}\times e^{-hf/k_BT}\,\overline{g_{\text{ff(fb)}}}\,(f,T), \tag{6.9}$$

$$\nu_{\text{ea}}=\frac{8\sqrt{2}}{3}N_0\left(\frac{kT}{\pi m}\right)^{1/2}(3c_{\text{tr}}k_BT+d_{\text{tr}}). \tag{6.10}$$

Here the exponential factor $\exp(-hf/k_BT)$ is commonly referred to as the Cillie exponential factor [43]; $\overline{g_{\text{ff}}}(f,T)$ and $\overline{g_{\text{fb}}}(f,T)$ are the velocity-averaged free-free and free-bound Gaunt factor, respectively, [44]

$$\overline{g_{\text{ff}}}(f,T)=\frac{e^{hf/k_BT}}{k_BT}\int_{hf}^\infty dE\, g_{\text{ff}}(f,E)e^{-E/k_BT}, \tag{6.11}$$

$$\overline{g_{\text{fb}}}(f,T)=2x_1\sum_{n^*}^{\infty}\frac{1}{n^3}e^{x_n}g_{\text{fb}}(n,f,v). \tag{6.12}$$

In Eq. (6.12), $x_n=E_{\text{ion}}/n^2k_BT$, with E_{ion} being the first ionization energy of the atom, and n^* is the lowest level for which $E_{n^*}<hf$.

Note that, assuming g_{ff}, $g_{\text{fb}}\simeq 1$, the above equations can be reduced to

$$\overline{g_{\text{ff}}}(f,T)=1, \tag{6.13}$$

$$\overline{g_{\text{fb}}}(f,T)=2x_1\sum_{n^*}^{\infty}\frac{1}{n^3}e^{x_n}. \tag{6.14}$$

The summation in Eq. (6.14) can be further simplified if the photon energy is small compared with the ionization energy, so that the energy level n^* is high in comparison with the ground state, as is the case for argon [20]. Since the density of the levels increases rapidly with increasing n, the discrete levels higher than n^* can be replaced by a continuous spectrum and the summation replaced by an integration, and Eq. (6.14) simplifies to

$$\overline{g_{\text{fb}}}(f,T)=e^{hf/k_BT}-1=e^{hc/k_BT\max\{\lambda,\lambda_2\}}-1. \tag{6.15}$$

As the absorption coefficient κ is related to the effective collision frequency as

$$\kappa=\left(\frac{\omega_p}{\omega}\right)^2\frac{\nu}{c}, \tag{6.16}$$

we can find the absorption coefficients corresponding to Eqs. (6.9) and (6.10)

$$\kappa_{\text{ei(rc)}}=\frac{4}{3}\left(\frac{2\pi}{3mk_BT}\right)^{1/2}\frac{Z^2N_i^2e^6\lambda^2}{(4\pi\epsilon_0)^3k_BTc^3m}\times e^{-hf/k_BT}\,\overline{g_{\text{ff(fb)}}}\,(f,T), \tag{6.17}$$

$$\kappa_{\text{ea}}=8\sqrt{2}\frac{N_iN_0e^2\lambda^2}{4\pi\epsilon_0c^3}\left(\frac{k_BT}{\pi m}\right)^{3/2}\times\left(c_{\text{tr}}+\frac{d_{\text{tr}}}{3k_BT}\right). \tag{6.18}$$

The absorption coefficient $\kappa_{\text{ei(rc)}}$ in Ref. [20] differs from ours in two ways. (i) They differ by a factor of k_BT/hf. However, this difference is not very significant as $k_BT\simeq hf$ in SL; (ii) For electron-ion bremsstrahlung, the free-free Gaunt factor and the Cillie exponential correction were neglected in Ref. [20]. As we will discuss later (see Fig. 7), this could result in a factor of 3 difference in the calculated spectra.

In the present paper, we explicitly take account of all Gaunt factors and the exponential correction, in particular we adopt the fitting formula proposed by Nozawa *et al.* [45] and Itoh *et al.* [46] to compute the average free-free Gaunt factor. For the free-bound Gaunt factor, since the photon energies 1.5–6.2 eV, corresponding to the wavelength 200–800 nm, is small compared with the ionization energy ($E_{\text{ion}}=15.8$ eV for argon), Eq. (6.15) is still a good approximation and we retain it for computing the average free-bound Gaunt factor. As a remark, following Eqs. (6.9), (6.13), and (6.15) we have $\nu_{\text{rc}}/\nu_{\text{ei}}\simeq e^{hf/k_BT}-1$, hence electron-ion bremsstrahlung is more dominant over recombination when $hf\ll k_BT$. For SL, however, both processes are important since the thermal energy is typically $\sim$1.7–4.3 eV.

For the purpose of comparison, in the following discussion we will use two different sets of formulas, respectively denoted by P1 and P2 models, to calculate the collision frequencies. The P1 model employs the free-bound Gaunt factor, but ignore the free-free Gaunt factor and the Cillie exponential cut-off factor

$$\nu_{\text{ei}}=2\left(\frac{2\pi}{3}\right)^{3/2}N_i\left(\frac{Ze^2}{4\pi\epsilon_0k_BT}\right)^2\left(\frac{k_BT}{m}\right)^{1/2}\frac{k_BT}{hf} \tag{6.19}$$

$$\nu_{\text{rc}}=2\left(\frac{2\pi}{3}\right)^{3/2}N_i\left(\frac{Ze^2}{4\pi\epsilon_0k_BT}\right)^2\left(\frac{k_BT}{m}\right)^{1/2}\frac{k_BT}{hf}\,\overline{g_{\text{fb}}}\,(f,T), \tag{6.20}$$

$$\nu_{\text{ea}}=\frac{8\sqrt{2}}{3}N_a\left(\frac{k_BT}{\pi m}\right)^{1/2}(3c_{\text{tr}}k_BT+d_{\text{tr}}). \tag{6.21}$$

Through Eq. (6.16), it is obvious that this set of formulas for the collision frequencies are consistent with the set of absorption coefficients used in [20,21].

By contrast, the P2 model, derived earlier in this section, readily takes account of free-bound Gaunt factor, free-free Gaunt factor, and exponential cut-off factor

$$\nu_{\text{ei}}=2\left(\frac{2\pi}{3}\right)^{3/2}N_i\left(\frac{Ze^2}{4\pi\epsilon_0k_BT}\right)^2\left(\frac{k_BT}{m}\right)^{1/2}e^{-hf/k_BT}\,\overline{g_{\text{ff}}}\,(f,T), \tag{6.22}$$

$$\nu_{\rm rc} = 2\left(\frac{2\pi}{3}\right)^{3/2} N_i \left(\frac{Ze^2}{4\pi\epsilon_0 k_B T}\right)^2 \left(\frac{k_B T}{m}\right)^{1/2} e^{-hf/k_B T}\, \overline{g_{\rm fb}}\,(f,T), \tag{6.23}$$

$$\nu_{\rm ea} = \frac{8\sqrt{2}}{3} N_a \left(\frac{k_B T}{\pi m}\right)^{1/2} (3c_{\rm tr} k_B T + d_{\rm tr}). \tag{6.24}$$

Finally we state the basic assumptions underpinning the above formulas for plasma collision processes: (1) The plasma is "cold" meaning that the electron thermal velocity is negligible with respect to the phase velocity of the wave, $v_{\rm th} \ll v_{\rm ph}$; (2) the plasma is in the weak coupling regime, i.e., the ions are weakly interacting during their thermal motions. It is customary to indicate the degree of coupling by the dimensionless ion-coupling parameter (see, e.g., [47])

$$\Gamma = \frac{Z^2 e^2}{4\pi\epsilon_0 R_{\rm ion} k_B T}, \tag{6.25}$$

with $R_{\rm ion} = (4\pi N_i/3)^{-1/3}$ being the mean interionic distance. If $\Gamma \ll 1$, the system is said to be weakly coupled; on the other hand if $\Gamma \gtrsim 1$, the system is in the strong coupling regime [47]. We find $\Gamma \lesssim 1$ in a typical SL bubble (Sec. VIII), hence the assumption of weak coupling is at least approximately satisfied.

VII. COMPUTATIONAL FLUID MECHANICS

In this section, we summarize the CFM used in the present paper, which was developed by Yuan *et al.* [14] and Cheng *et al.* [15] and later extended by Ho *et al.* [35] to include the ionization and recombination processes. The model couples the Rayleigh-Plesset (RP) equation for the bubble wall with the Navier-Stokes (NS) equations for the gas (including all the charged species resulting from ionizations), while independently solving the energy equation for the surrounding water. The number densities of the charged species are computed from the reaction rates approach. The effects of viscosity, surface tension, equation of state (EOS), compressibility and thermal conductivity of the ambient liquid are also taken into account.

A. Bubble-wall dynamics

To account for the effect of liquid compressibility, a more robust RP equation that gives the bubble radius R as a function of time t is used [14,15,35,48]

$$\frac{1-M}{1+M} R\ddot{R} + \frac{3-M}{2(1+M)} \dot{R}^2 = H_l - \frac{P_s(t')}{\rho_0} + \frac{t_R \dot{H}_l}{1+M}. \tag{7.1}$$

Here $t_R \equiv R/c_l$, with c_l the speed of sound in the surrounding liquid, $M \equiv \dot{R}/c_l$, $t' \equiv t + t_R$, ρ_0 is the ambient liquid density, and $P_s(t') = -P_a \sin(\omega t')$ is the sonic driving pressure with frequency ω and amplitude P_a. Also, the enthalpy H_l and the speed of sound of the liquid and c_l are given by

$$H_l = \int_{P_0}^{P_l} \frac{{\rm d}P_l}{\rho_l}, \tag{7.2}$$

$$c_l^2 = \frac{{\rm d}P_l}{{\rm d}\rho_l}. \tag{7.3}$$

This modified RP equation includes terms to first order in the Mach number M of the bubble wall and allows for a variable c_l.

Combining Eqs. (7.2) and (7.3) with the EOS of the ambient liquid in the modified Tait form [49]

$$\frac{P_l + B}{P_0 + B} = \left(\frac{\rho_l}{\rho_0}\right)^n, \tag{7.4}$$

yields the explicit forms for H_l and c_l

$$H_l = \frac{n}{n-1}\left(\frac{P_l + B}{\rho_l} - \frac{P_0 + B}{\rho_0}\right), \tag{7.5}$$

$$c_l^2 = \frac{n(P_l + B)}{\rho_l}, \tag{7.6}$$

where $B = 3049.13$ bar and $n = 7.15$ are valid for water up to 10^5 bar.

Equations (7.1), (7.5), and (7.6) must be supplemented by the boundary condition at the bubble wall, namely, that the pressure $P_l(t)$ on the liquid side of the gas-liquid interface differs from the pressure $P(R,t)$ on the gas side of the gas-liquid interface by the effects of surface tension and the normal component of viscous stresses [49]

$$P(R,t) - \tau_{rr}|_{r=R} = P_l(t) + \frac{4\eta_l \dot{R}}{R} + \frac{2\sigma}{R}. \tag{7.7}$$

B. Hydrodynamics of gas

The conservation of mass, momentum, and energy for the gas flow in the spherical bubble is described by the compressible NS equations. They can be rewritten into a conservative form with source terms as

$$\frac{\partial \rho}{\partial t} + \frac{\partial}{\partial r}(\rho v) = -\frac{2\rho v}{r}, \tag{7.8}$$

$$\frac{\partial(\rho v)}{\partial t} + \frac{\partial}{\partial r}(\rho v^2 + P) = -\frac{2\rho v^2}{r} + \frac{1}{r^2}\frac{\partial}{\partial r}(r^2 \tau_{rr}) + \frac{\tau_{rr}}{r}, \tag{7.9}$$

$$\frac{\partial(\rho E)}{\partial t} + \frac{\partial}{\partial r}(\rho E + P)v = -\frac{2(\rho E + P)v}{r} + \frac{1}{r^2}\frac{\partial}{\partial r} \times \left[r^2\left(v\tau_{rr} + k\frac{\partial T}{\partial r}\right)\right]. \tag{7.10}$$

Here r, ρ, v, P, T, τ_{rr}, k e, and $E = e + v^2/2$ are the radial distance from the center of the bubble, gas density, radial velocity, pressure, temperature, normal viscous stress, coefficient of thermal conductivity, the internal energy, and total energy per unit mass, respectively.

If, due to ionizations and recombinations, there exists N_s species inside the bubble, then $N_s - 1$ mass conservation

equations for these species must be supplemented with Eqs. (7.8)–(7.10). In Ref. [35], the maximum ionization level of the gas atom is taken to be 5, making a total of $N_s=7$ species inside the bubble. This is more than adequate for the present temperature range; in fact, Ho *et al.* [35] have shown that even the second ionization level can be safely ignored in practice. Note, since the ion densities change due to ionizations and recombinations, source terms must be added to the right-hand side of the conservation equations.

For convenience, let f_j be the mass fraction of Ar^{j+} (with $j=0,1,2,3,4,5$) or electrons (with $j=e$), so that $\Sigma_{j=e,0}^{5} f_j=1$. Therefore ρf_j represents the mass density of an individual species. The number density of an individual species is related to its mass fraction by $n_j=\rho f_j/m_j$, where m_j is the mass of an atom ($j=0$), or an ion with a charge j ($j=1-5$), or an electron ($j=e$). The mass conservation equations of the species is then given by

$$\frac{\partial(\rho f_j)}{\partial t}+\frac{\partial}{\partial r}(\rho f_j v)=-\frac{2\rho f_j v}{r}+(S_s)_j. \tag{7.11}$$

Here, the extra term $(S_s)_j$ is the source term for ρf_j which arises from ionization and recombination processes. It depends on the net rate of change of the number density of the species $\dot{n}_j$ through

$$(S_s)_j=m_j\dot{n}_j. \tag{7.12}$$

For the ions ($j=0,1,2,3,4,5$), the net rate of change is given by

$$\dot{n_j}=n_{j-1}n_e\alpha_{j-1\to j}^{\text{ion}}-n_jn_e\alpha_{j\to j+1}^{\text{ion}}+n_{j+1}n_e(\alpha_{j+1\to j}^{\text{rrec}}+\alpha_{j+1\to j}^{\text{trec}})-n_jn_e(\alpha_{j\to j-1}^{\text{rrec}}+\alpha_{j\to j-1}^{\text{trec}}), \tag{7.13}$$

where $\alpha_{j\to j+1}^{\text{ion}}$, $\alpha_{j\to j-1}^{\text{rrec}}$, and $\alpha_{j\to j-1}^{\text{trec}}$ are the rates of ionization, radiative recombination, and three-body recombination of particles with a charge of j, respectively. The formulas for these rates can be found in [50].

The net rate of change of the number density of electrons is simply given by charge conservation. Now that

$$f_e=1-\sum_{j=0}^{5} f_j, \tag{7.14}$$

taking time derivative and multiplying both sides by ρ gives

$$(S_s)_e=-\sum_{j=0}^{5}(S_s)_j. \tag{7.15}$$

C. Equation of state of gas

The hydrodynamics of the bubble is certainly affected by the EOS. The most widely used van der Waals EOS can be modified to take into account the ionization processes [19]

$$P=\left(\sum_{j=0}^{5}\frac{f_j}{m_j}+\frac{f_e}{m_e}\right)\frac{k_B\rho T}{1-b\rho}, \tag{7.16}$$

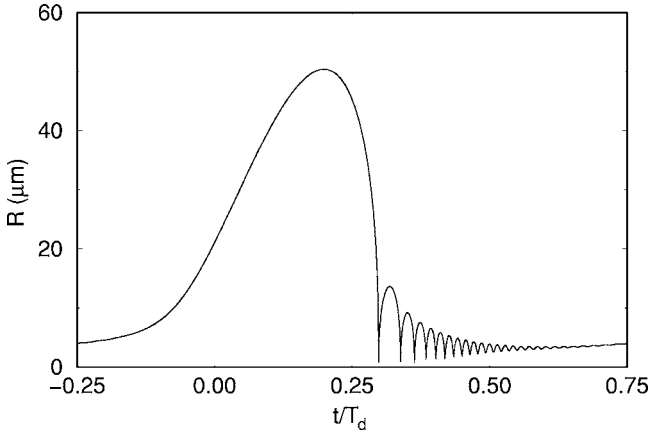

FIG. 3. A plot of the bubble radius R versus time t, which is normalized with respect to the acoustic period T_d.

$$e=\frac{3}{2}k_BT\left(\sum_{j=0}^{5}\frac{f_j}{m_j}+\frac{f_e}{m_e}\right)+k_B\sum_{j=1}^{5}\sum_{i=j}^{5}\frac{f_i}{m_i}T_j, \tag{7.17}$$

where T_j is the ionization energy of an ion with charge $j-1$, and b the excluded volume. This EOS is denoted as MVEOS.

The physical meanings of the MVEOS, Eqs. (7.16) and (7.17), are manifest. The total pressure P is the sum of the contributions by different species, which are separately taken into account in proportion to their abundances. The internal energy e of the gas consists of both the thermal energy (the first term) and ionization energy (the second term).

D. Energy transport in the liquid

The changes in the liquid temperature T_l is accounted for with the assumption that the liquid compressibility and viscosity do not affect the heat transfer process between the bubble and the surrounding water. As such, the energy equation for the water is

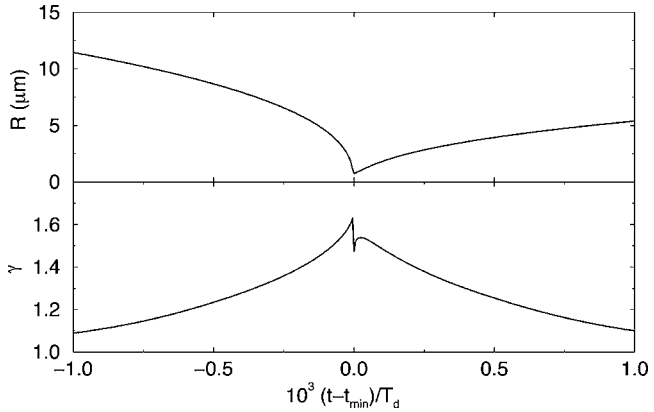

FIG. 4. The bubble radius R (upper panel) and the polytropic exponent γ (lower panel) are plotted against the normalized time $10^3(t-t_{\min})/T_d$, where $t_{\min}$ is the moment at which R attains its minimum value of about 0.7 μm.

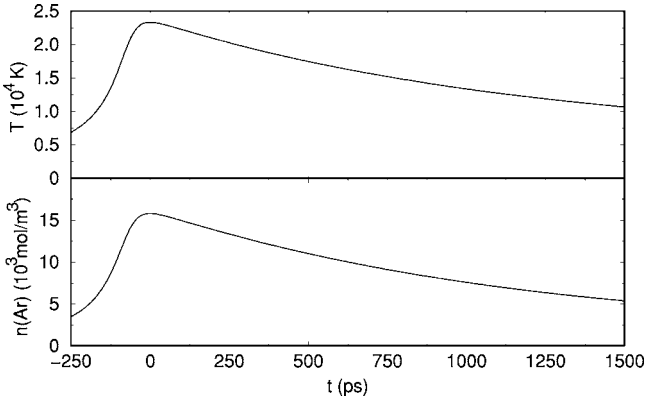

FIG. 5. Time profiles of temperature T (upper panel) and number density of argon atom n_0 (lower panel) near the instant of minimum bubble size.

$$\frac{\partial T_l}{\partial t} + v_l \frac{\partial T_l}{\partial r} = D_l \frac{1}{r^2} \frac{\partial}{\partial r}\left(r^2 \frac{\partial T_l}{\partial r} \right), \tag{7.18}$$

where v_l and D_l are the velocity and thermal diffusion coefficient of the liquid, respectively.

VIII. NUMERICAL RESULTS

In order to elucidate the significance of individual physical factors affecting SBSL, in the following we present and compare numerical results obtained from simulations constructed with different models. Specifically, we consider (i) UBM versus CFM model; (ii) GOM versus WOM; and (iii) the two plasma models, P1 versus P2.

The rest of this section is organized as follows: First we study how the effects of various physical entities, including plasma, wave, and temperature, can affect the emitted light pulse using the simple UBM model. Then we use the CFM model that is more realistic to mimic SBSL and compare relevant numerical results with those of UBM.

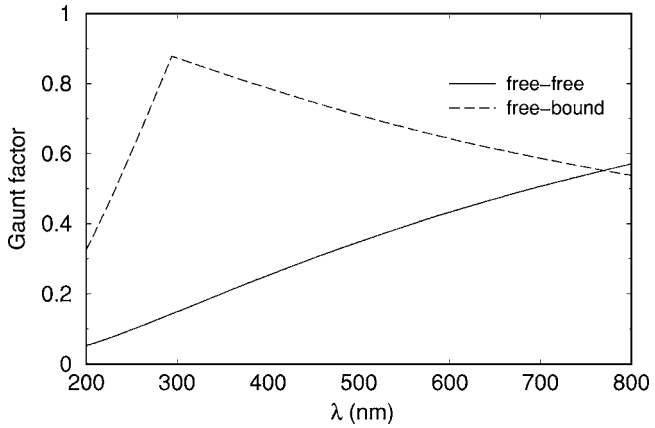

FIG. 6. Free-free (solid line) and free-bound (dashed line) Gaunt factors multiplied by the Cillie exponential factor at the instant of minimum bubble size.

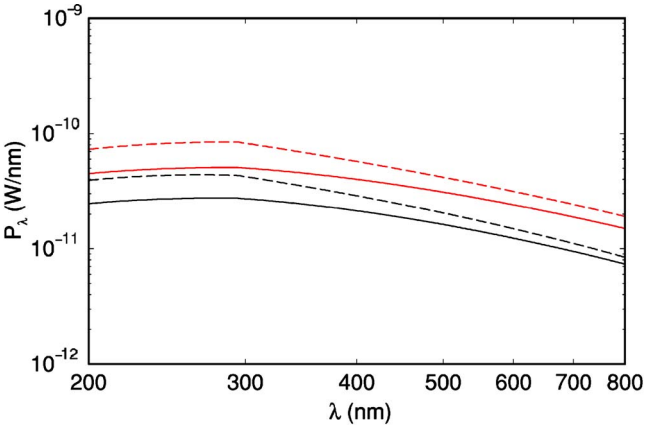

FIG. 7. (Color online) The spectral radiance P_λ is plotted against the wavelength λ for the following models: GOM+P1 (grey-dashed line), GOM+P2 (grey-solid line), WOM+P1 (dark-dashed line), and WOM+P2 (dark-solid line).

A. Emission in Uniform Bubble Model

UBM here refers to the model used in [20,21], where the RP equation assumed incompressibility of the surrounding liquid and a variable polytropic exponent $\gamma(R,\dot{R},T)$ was used to account for effects of thermal conduction. However, instead of using the fitting formula in [20] for computing the polytropic exponent $\gamma(R,\dot{R},T)$, we employed the formula proposed in [51] in the simulations. As in Ref. [20], we studied the oscillations of a bubble with ambient radius $R_0 = 5.0\ \mu$m, subjected to an ultrasonic wave with $f = 20$ kHz and $P_a = 1.3$ atm. Figures 3 and 4, respectively, show for the UBM the time evolutions of the bubble radius R over one acoustic cycle and, in the vicinity of the maximum bubble compression, the radius and the polytropic exponent γ. The number density of argon atoms and the temperature near the instant of minimum radius are shown in Fig. 5. Here we remark that the temperature profile is slightly different from that in [20] due to the difference in the formulas for $\gamma(R,\dot{R},T)$. The profile remains essentially the same, but the

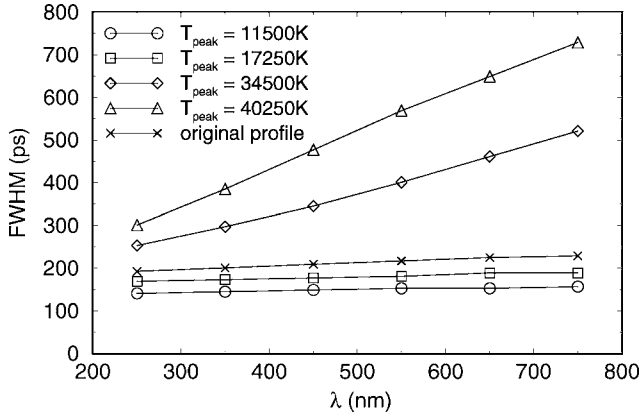

FIG. 8. FWHM obtained from UBM+GOM versus wavelength λ. Lines with circles, squares, crosses, diamonds and triangles, respectively, represent the cases with a scaling of 0.5; 0.75; 1 (i.e., no scaling); 1.50; and 1.75.

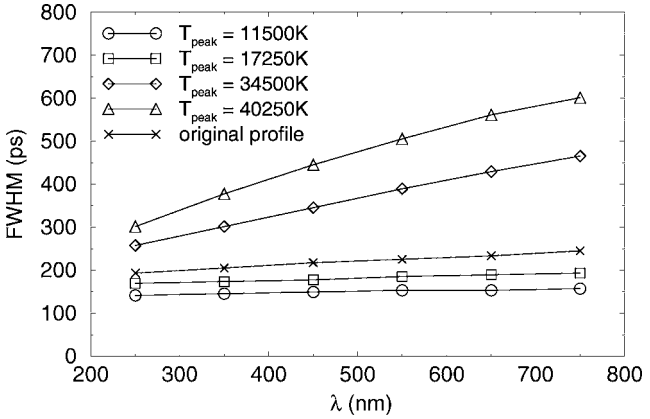

FIG. 9. FWHM obtained from UBM+WOM versus wavelength λ. Lines with circles, squares, crosses, diamonds, and triangles, respectively, represent the cases with a scaling of 0.5; 0.75; 1 (i.e., no scaling); 1.50; and 1.75.

peak temperature in our result is about 3000 K higher. The temperature and density profiles are used as inputs in our calculations of the spectral radiance, from which other light emission properties [e.g., pulse shapes and full width at half maximum (FWHM)] are obtained.

1. Plasma and wave effects

As mentioned previously, we employed two plasma collision models P1 and P2 in the simulations. The differences in these two models originate from the free-free (or free-bound) Gaunt factor and the Cillie exponential cut-off factor $\exp(-hf/k_BT)$. The exponential factor is usually close to unity in the Rayleigh-Jeans limit where $hf \ll k_BT$, but for the case of SL, k_BT is of the order of a few electron volts and is within the range 1.5–6.2 eV of the observed light spectrum, and hence is not negligible. In particular we find, when the bubble is at minimum size and the temperature and density of its contents are also at their maxima, the free-free Gaunt factor and the free-bound Gaunt factors, multiplied by the exponential cutoff, result in a correction factor of order 0.1 (see Fig. 6). Figure 7 shows the computed power spectra

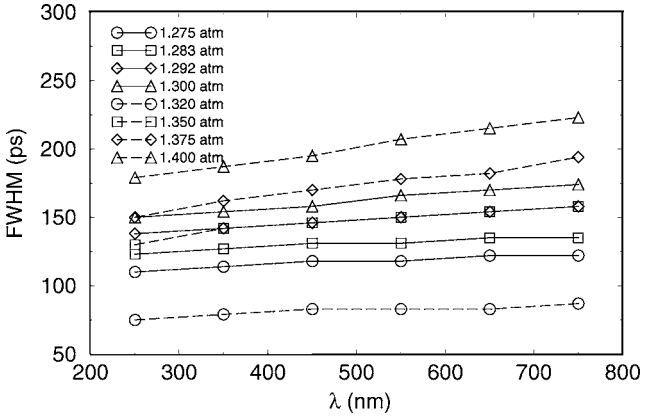

FIG. 10. FWHM versus wavelength λ calculated from UBM +WOM. Cases with $T=20$ °C and $T=2.5$ °C are indicated by the solid curve and the dashed curve, respectively.

TABLE I. Driving pressure P_a and ambient radius R_0 at $T_0=20$ °C and $T_0=2.5$ °C that give stable sonoluminescing bubble for $f=26.5$ kHz.

		$T_0=20$ °C		
P_a (atm)	1.275	1.283	1.292	1.300
R_0 (μm)	2.9	3.2	3.6	3.9
		$T_0=2.5$ °C		
P_a (atm)	1.320	1.350	1.375	1.400
R_0 (μm)	2.0	3.5	4.0	4.5

obtained from simulations constructed respectively with GOM/WOM+P1/P2, clearly demonstrating that the P2 model indeed leads to an decrease in the radiance.

Furthermore, we can observe in Fig. 7 that the power is overestimated when GOM is used rather than WOM, which can be readily explained as follows. When a plane wave is incident on a WOM bubble, part of it is reflected or scattered from the boundaries and the remaining part is absorbed as heat. In light of Kirchhoff's law then, less absorption implies less emission. In contrast, reflection and diffraction are neglected in GOM, resulting in an overestimated absorption and hence emission. Therefore, to achieve realistic power calculations comparable with experimental results, the effects of both the wave nature of light and the Gaunt factor correction cannot be neglected, consistent with the point we made earlier.

In subsequent discussions we will employ two specific light emission models: The model proposed in Ref. [20] (GOM+P1) and our present model (WOM+P2), and it should be understood that all power computations employing GOM are done with P1 while those employing WOM are done with P2.

2. Temperature effects

For our case studied here using the UBM model, the maximum temperature achieved at the instant of minimum bubble size is about 23 000 K (Fig. 5). To study the effect of the interior temperature on light emission, we scale by hand the original temperature profile for $P_a=1.300$ atm and $R_0=5.0$ μm by some chosen factors, say $0.3, 0.5, 0.75, 1.5$, and 1.75, while keeping the densities of Ar neutrals constant. Accordingly, two of the three input parameters to the light emission model (temperature and ion number density) are changed and one (the atom number density) remains fixed. We employ both GOM and WOM to calculate the power, and study the spectral variation of the FWHM calculated

TABLE II. Driving pressure P_a and ambient radius R_0 at $T_0=20$ °C that give stable sonoluminescing bubble for $f=20$ kHz.

P_a (atm)	1.275	1.300	1.325	1.350
R_0 (μm)	2.6	4.0	4.7	5.4

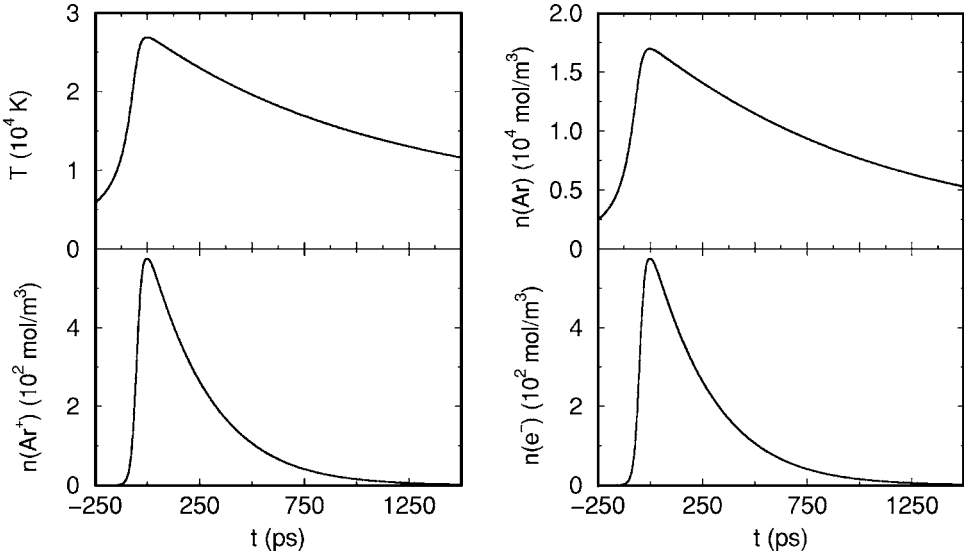

FIG. 11. Temperature T, number densities of argon neutrals $n(\mathrm{Ar})$, ions $n(\mathrm{Ar}^+)$, and electrons $n(\mathrm{e}^-)$ shown as a function of time, where $t=0$ is the instant of minimum bubble radius, for a UBM bubble with $P_a=1.325$ atm, and $R_0=4.7$ μm.

within 100 nm wavelength windows as shown in Figs. 8 and 9. It is remarkable that a consistently smaller spectral variation of the FWHM is obtained when the light emission model WOM is used. The unscaled profile is about constant over the range of wavelength considered as in Ref. [20], which employed UBM and GOM, and the profile still remains remarkably constant when the temperature was scaled down by a factor of 0.5 and 0.75 (to a peak temperature of about 10 000–20 000 K). Scaling down by 0.3 (to a peak temperature of about 7000 K) produced zero power output since the temperature was much lower than that required for ionization. Nevertheless, scaling up by 1.5 and 1.75 (to a peak temperature of about 35 000–45 000 K) produces dramatic variation of the FWHM. Hence, we find that the spectral uniformity of the FWHM holds only when the SL bubble temperature is restricted within a rather small range of moderate values. However, we remark that the temperature is underestimated in the UBM since local temperature rises were not taken account of. With a more realistic hydrodynamic modeling, Ref. [35] found the temperature should be several 10^4 K higher. Thus, we expect that a larger FWHM spectral variation with increased driving pressure will be an essential realistic feature of SL.

In addition, we have studied the effect of ambient water temperature on SL light emission, using WOM and the values of (P_a, R_0) extracted from the phase diagram in Ref. [52], at $T_0=20$ °C and 2.5 °C and at a driving frequency of $f=26.5$ kHz. Here we observe from Fig. 10 the general trend of a larger FWHM toward the red end of the spectrum as the pressure is tuned up, and this increase is further enhanced at a lower water temperature. This is consistent with the experimental findings of Moran and Sweider [6] and is readily explained. At a lower water temperature, the bubble can be driven harder [52] so that, given a certain value of ambient radius, a larger driving pressure can be applied while maintaining bubble stability. The bubble collapses more violently under the larger pressure and hence the temperature of the bubble interior achieves a higher value, resulting in a larger FWHM spectral variation. Therefore, in effect, both of our observations under increased driving pressure and lower water temperature can be explained in terms of the higher temperature reached inside the bubble. (See Table I.)

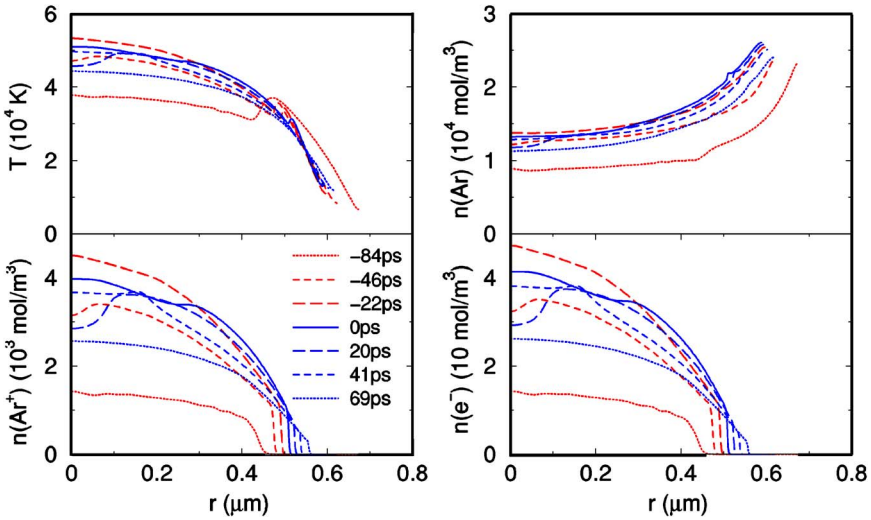

FIG. 12. (Color online) Snapshots near the instant of minimum bubble radius ($t=0$) for the same quantities as in Fig. 11 plotted against radial distance, for a CFM bubble with $P_a=1.325$ atm, and $R_0=4.7$ μm. Grey lines indicate times before zero while dark lines indicate times after zero.

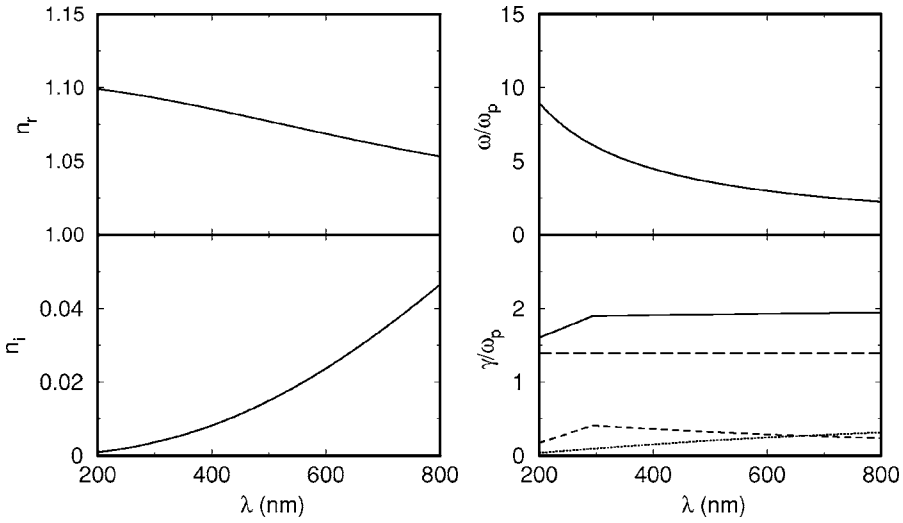

FIG. 13. Shown on the left are the real part n_R and imaginary part n_I of the refractive index, on the right are the ratios ω/ω_p and ν/ω_p versus the wavelength λ for a UBM bubble with $P_a=1.375$ atm and $R_0=2.6$ μm at the instant of minimum radius. In the graph ν/ω_p versus λ, the dotted, short-dashed, long-dashed, and full lines, respectively, show, ν_{ei}, ν_{rc}, ν_{ea}, and ν.

B. Computational Fluid Mechanics Model

1. Hydrodynamics

Now we employ CFM developed by Ho *et al.* [35] that includes the effects of ionizations and recombinations to calculate the power spectra and pulse profiles using WOM, and compare the results with those obtained from joint application of UBM and GOM. The set of conditions that we employ is extracted from Ref. [20] and shown in Table II, where $T_0=20$ °C, $f=20$ kHz and the dissolved gas concentration is 0.20%. Figures 11 and 12, respectively, show the computed results of UBM and CFM for a case with $P_a=1.325$ atm, $R_0=4.7$ μm. It is found that the maximum temperature obtained with CFM can exceed 5×10^4 K while that in UBM is less than 3×10^4 K. Accordingly, the number of Ar^+ ion in CFM is much greater than that in UBM.

2. Light emission

To apply WOM to CFM, which produces an inhomogeneous profile of bubble temperature and number densities, we approximate the resultant inhomogeneous profile by a layered one and use within each layer j the average values of the temperature, the number densities of atom and electron there. The absorption coefficient $\kappa(j)$, collision frequency $\gamma(j)$, and refractive index $n(j)$ can accordingly be computed using these averaged values. This approximation scheme allows for the application of WOM to the resulting multilayered spherical configuration.

As the degree of ionization in CFM result is much higher than that in UBM, the difference in the optical properties of these two models is obvious. As shown in Figs. 13 and 14, ω/ω_p is reduced by a factor of 2.5 in CFM as compared to UBM. In particular, in CFM ω/ω_p is close to unity near the UV end, indicating that plasma collective effects may be significant in the short-wavelength regime. Also, both dispersion and absorption are considerably stronger in the CFM case, exhibiting a larger variation in n_R and a larger n_I than the UBM case.

In Sec. VI B we have made the assumption that the plasma is so tenuous that the Coulomb energy is much smaller than the average thermal energy of individual particles and the plasma behaves like an ideal gas. The values of the ion-coupling parameter Γ at the instant of maximum bubble compression for the cases studied here (see Table II) are shown in Fig. 15. For UBM we note that $\Gamma\simeq0.7$ for all four cases. In the CFM bubble, interestingly there is a clear

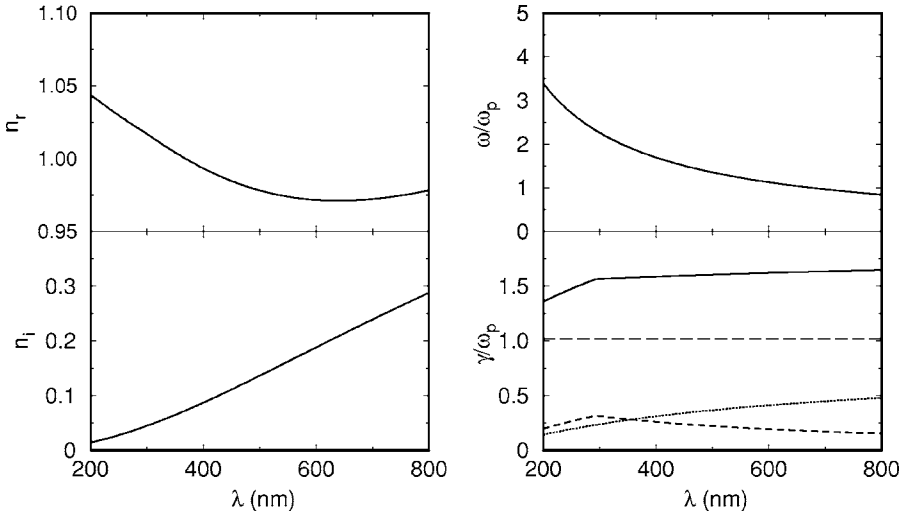

FIG. 14. Same as Fig. 13, for a CFM bubble with $P_a=1.325$ atm, and $R_0=4.7$ μm. The quantities shown here are those of the innermost layer which occupies the inner 7.5% of the bubble radius for $P_a=1.325$ atm hence is representative of the hottest and densest region of the bubble.

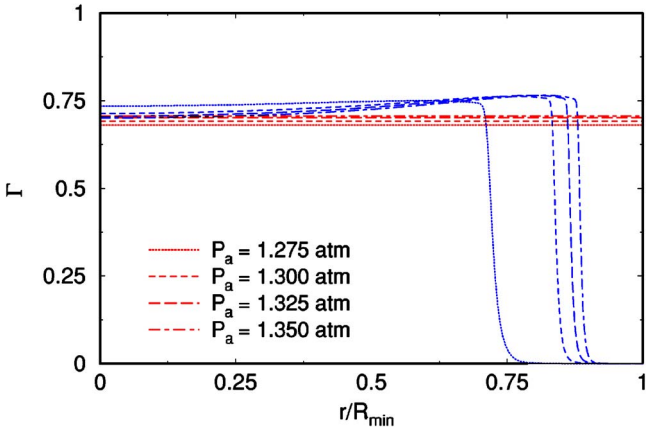

FIG. 15. (Color online) The ion-coupling parameter Γ is plotted against r, normalized by the minimum radius $R_{\min}$ at the instant of maximal bubble compression. The values obtained from UBM (CFM) are indicated by grey (dark) lines.

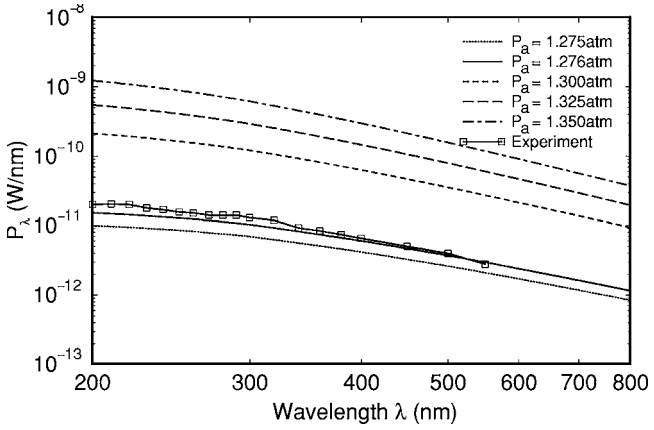

FIG. 17. Spectral radiance P_λ versus wavelength λ obtained from WOM+CFM+P2. The best fit for the experimental spectrum [1] is indicated by the solid line, in which P_a=1.276 atm, R_0 =2.7 μm.

formation of two regions: an inner core which is moderately coupled $\Gamma \sim 0.7$ and an outer shell which is weakly coupled $\Gamma \simeq 0$. In addition the effect of increasing the driving pressure is seen to increase the size of this moderately coupled inner core. Since the degree of coupling is moderate and not too strong, we expect that the formulas used for the absorption coefficients and collision frequencies based on the tenuous plasma assumption should still apply. However, on the other hand, if the driving pressure increases while maintaining the stability of oscillation, it is likely that the plasma might become a nonideal one. The physical property of such dense nonideal plasma is rather complicated and is beyond the scope of the present paper [47].

In the following we contrast data obtained, respectively, from GOM+UBM and WOM+CFM and specifically consider three different physical quantities, namely, the spectrum, the pulse shape, and the FWHM of light pulses.

In Figs. 16 and 17 we show the computed spectra using GOM+UBM+P1 and WOM+CFM+P2, respectively. One clearly sees the improvement (Fig. 17) of our refined model, namely, WOM+CFM+P2, that the calculated spectral shape is much closer to the experimental results [1] than the GOM+UBM+P1 model. In particular, major improvement is seen in the UV portion of the spectrum.

The calculated pulse shapes are shown in Figs. 18 and 19, respectively, evidently the pulse shapes produced from WOM+CFM+P2 are more consistent with experimental data [4,6,53] where the long-time tail was not observed. By contrast, as shown Fig. 18, a long-time tail appears in GOM+UBM+P1 and is an undesirable feature.

Figure 20 shows the calculated FWHM plotted against the wavelength for both cases. While it is clear that the FWHM increases with driving pressure as found in experiments [4,6,53], we also see that the FWHM remains nearly a constant over 200–800 nm *only* at a low pressure P_a $\sim$1.275 atm even in the more realistic WOM+CFM+P2 model (c.f. Sec. VIII A 2). We remark that the results obtained by Gompf *et al.* [4] showing similar pulse widths for the red and UV pulse were obtained under a driving pressure of P_a=1.200 atm; which is smaller than the lowest pressure P_a=1.275 atm we used and is therefore expected to show a

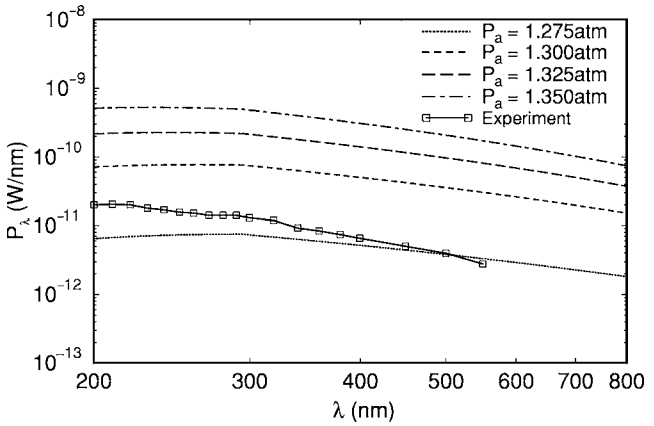

FIG. 16. Spectral radiance P_λ versus wavelength λ obtained from GOM+UBM+P1. The experimental spectrum is obtained from Barber *et al.* [1].

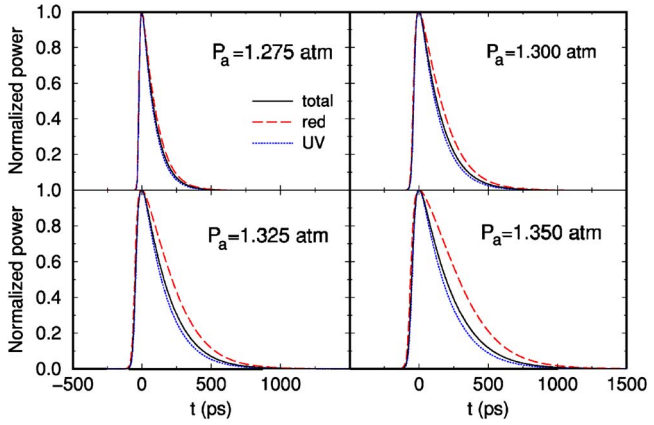

FIG. 18. (Color online) Normalized power versus time obtained from GOM+UBM+P1. The solid, dashed, and dotted lines are, respectively, the total normalized power, the normalized powers in the red and UV regions.

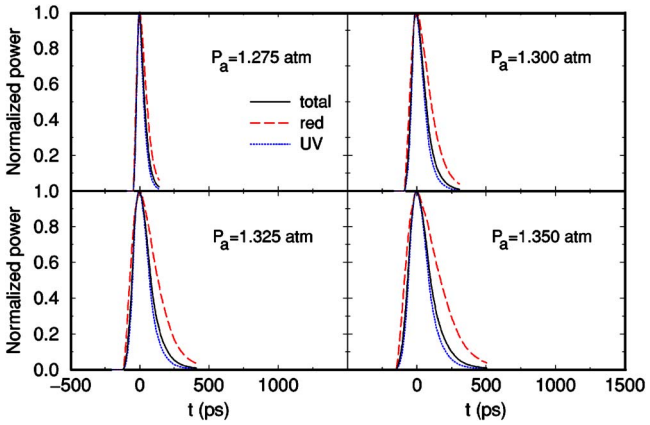

FIG. 19. (Color online) Normalized power versus time obtained from WOM+CFM+P2. The solid, dashed, and dotted lines are, respectively, the total normalized power, the normalized powers in the red and UV regions.

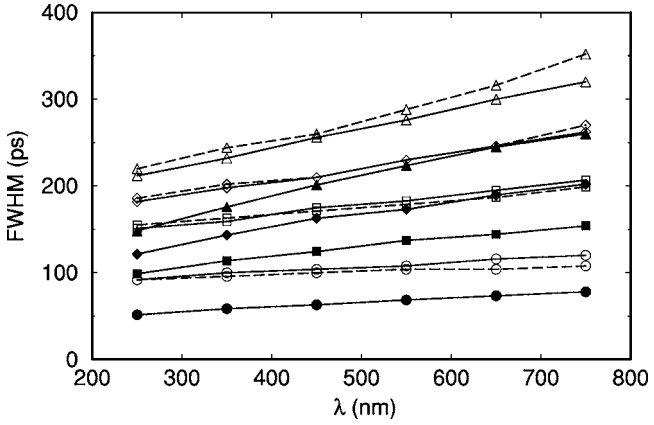

FIG. 20. FWHM of light pulse versus wavelength λ obtained at different driving pressures: circle $P_a=1.275$ atm, square $P_a=1.300$ atm, diamond $P_a=1.325$ atm, and triangle $P_a=1.350$ atm. Dashed lines with empty symbols and solid lines with filled symbols are calculated from GOM+UBM+P1 and WOM+CFM+P2, respectively.

constant pulse width. In particular the results of Moran and Sweider [6] showed the FWHM increases with wavelength at a low ambient water temperature 3 °C, which, as remarked previously, also resulted in a larger driving pressure. Thus we emphasize that in general the notion of wavelength independence of the SL pulse width is only correct at low driving pressures; and at higher driving pressures spectral dispersion of the pulse width shows up, and this can be simply explained within our model. Either effects of higher driving pressure or lower water temperature boil down to the consequence of higher bubble temperature. As the bubble becomes hotter, both optical dispersion and absorption become more significant and hence the bubble becomes more optically opaque, approaching a blackbody surface emitter. Red light is then radiated for a longer duration than the UV since, throughout one cycle, the bubble can stay at a lower-temperature state for a longer duration. As a consequence, the pulse width increases toward the red end of the spectrum. In other words, the emitted light becomes more spectrally dispersive because of the increased absorption and dispersion in the plasma medium. In particular, the absorption is highest (Figs. 13 and 14) at the red end of the spectrum, resulting in a flatter pulse shape there (larger FWHM). Thus, besides using a lower ambient temperature as in Ref. [6], if a strong enough pressure is applied (while still maintaining bubble stability) the spectral variation of the FWHM would be an observable consequence in experiment.

IX. CONCLUSION

In summary, we have proposed in the present paper a robust theory for optical emission in SBSL that properly takes into account of the wave nature and propagation of light in the absorptive plasma formed inside a sonoluminescing bubble in a self-consistent way. In addition, our theory can be applied to bubbles with inhomogeneous density and temperature profiles. The validity of our scheme was examined for the case of SBSL with argon bubbles. By introducing and implementing appropriate Gaunt factors and exponential correction in the collision frequencies; as well as the effects of optical thickness, scattering, reflection, and diffraction, our light emission model successfully explains the major features (including power spectrum, pulse shape, and FWHM) observed in SBSL experiments. In addition, the computed power spectra and pulse shapes are shown to be in excellent agreement with experimental results.

Besides, we have also shown that the experimentally observed spectral independence of the FWHM at $T_0=20$ °C is ascribable to the relatively small temperature range (about 10 000–30 000 K) achievable in a collapsing SL bubble. Above this range the bubble behaves in the way of a blackbody surface emitter and the spectral variation of the FWHM should be more notable. In fact, as the driving pressure goes up, the temperature reached inside the bubble rises. Also, if the ambient water temperature is lowered at a fixed ambient radius R_0, the driving pressure allowable for bubble stability extends to a larger value. This provides a theoretical explanation for why Moran and Sweider [6] found a spectral variation of the pulse width at $T=3$ °C.

Notwithstanding the above-mentioned achievements, the model developed in the present paper is only one of the many steps toward a better understanding of SBSL, which is an extremely complex phenomenon resulting from the subtle interplay of hydrodynamics, chemical reactions, plasma physics, and optics as well. Much more challenging problems, e.g., SBSL with inert gases other than argon and inclusion of water vapor in the hydrodynamic code, are still ahead for us. They are surely our goal of endeavor in the future.

ACKNOWLEDGMENTS

We thank M.-C. Chu and K. M. Pang for discussions. The work described in this paper was partially supported by a grant (Project No. 401603) from the Research Grants Council of the Hong Kong Special Administrative Region, China.

[1] B. P. Barber, R. A. Hiller, R. Löfstedt, S. J. Putterman, and K. R. Weninger, Phys. Rep. **281**, 65 (1997).
[2] M. P. Brenner, S. Hilgenfeldt, and D. Lohse, Rev. Mod. Phys. **74**, 425 (2002).
[3] B. P. Barber and S. J. Putterman, Nature (London) **352**, 318 (1991).
[4] B. Gompf, R. Gunther, G. Nick, R. Pecha, and W. Eisenmenger, Phys. Rev. Lett. **79**, 1405 (1997).
[5] R. A. Hiller, S. J. Putterman, and K. R. Weninger, Phys. Rev. Lett. **80**, 1090 (1998).
[6] M. J. Moran and D. Sweider, Phys. Rev. Lett. **80**, 4987 (1998).
[7] R. Hiller, S. J. Putterman, and B. P. Barber, Phys. Rev. Lett. **69**, 1182 (1992).
[8] R. Hiller, K. Weninger, S. J. Putterman, and B. P. Barber, Science **266**, 248 (1994).
[9] D. F. Gaitan, L. A. Crum, C. C. Church, and R. A. Roy, J. Acoust. Soc. Am. **91**, 3166 (1992).
[10] R. Löfstedt, B. B. Barber, and S. J. Putterman, Phys. Fluids A **5**, 2911 (1993).
[11] R. Löfstedt, K. Weninger, S. Putterman, and B. P. Barber, Phys. Rev. E **51**, 4400 (1995).
[12] C. C. Wu and P. H. Roberts, Phys. Rev. Lett. **70**, 3424 (1993).
[13] W. C. Moss, D. B. Clarke, and D. A. Young, Science **276**, 1398 (1997).
[14] L. Yuan, H. Y. Cheng, M.-C. Chu, and P. T. Leung, Phys. Rev. E **57**, 4265 (1998).
[15] H. Y. Cheng, M.-C. Chu, P. T. Leung, and L. Yuan, Phys. Rev. E **58**, R2705 (1998).
[16] W. C. Moss D. A. Young, J. A. Harte, J. L. Levatin, B. F. Rozsnyai, G. B. Zimmerman, and I. H. Zimmerman, Phys. Rev. E **59**, 2986 (1999).
[17] G. Vazquez, C. Camara, S. J. Putterman, and K. Weninger, Phys. Rev. Lett. **88**, 197402 (2002).
[18] G. Vazquez, C. Camara, S. J. Putterman, and K. Weninger, Opt. Lett. **26**, 575 (2001).
[19] N. Xu, L. Wang, and X. Hu, Phys. Rev. E **57**, 1615 (1998).
[20] S. Hilgenfeldt, S. Grossmann, and D. Lohse, Phys. Fluids **11**, 1318 (1999).
[21] S. Hilgenfeldt, S. Grossmann, and D. Lohse, Nature (London) **398**, 402 (1999).
[22] L. Frommhold and A. A. Atchley, Phys. Rev. Lett. **73**, 2883 (1994).
[23] L. Frommhold, Phys. Rev. E **58**, 1899 (1998).
[24] C. Eberlein, Phys. Rev. Lett. **76**, 3842 (1996).
[25] L. S. Bernstein and M. R. Zakin, J. Phys. Chem. A **99**, 14619 (1995).
[26] J. R. Willison, Phys. Rev. Lett. **81**, 5430 (1998).
[27] B. P. Barber, C. C. Wu, R. Löfstedt, P. H. Roberts, and S. J. Putterman, Phys. Rev. Lett. **72**, 1380 (1994).
[28] R. P. Taleyarkhan, C. D. West, J. S. Cho, J. R. T. Lahey, R. I. Nigmatulin, and R. C. Block, Science **295**, 1868 (2002).
[29] R. P. Taleyarkhan, J. S. Cho, C. D. West, R. T. Lahey, R. I. Nigmatulin, and R. C. Block, Phys. Rev. E **69**, 036109 (2004).
[30] S. J. Putterman, P. G. Evans, G. Vazquez, and K. Weninger, Nature (London) **409**, 782 (2001).
[31] C. Camara, S. Putterman, and E. Kirilov, Phys. Rev. Lett. **92**, 124301 (2005).
[32] S. D. Hopkins, S. J. Putterman, B. A. Kappus, K. S. Suslick, and C. G. Camara, Phys. Rev. Lett. **95**, 254301 (2005).
[33] D. J. Flannigan and K. S. Suslick, Nature (London) **434**, 52 (2005).
[34] S. M. Rytov, Y. A. Kravtsov, and V. I. Tatarskii, *Principles of Statistical Radiophysics 3: Elements of Random Fields* (Springer-Verlag, Berlin, 1989).
[35] C. Y. Ho, L. Yuan, M.-C. Chu, P. T. Leung, and W. Wei, Phys. Rev. E **65**, 041201 (2002).
[36] T. W. Chen, P. T. Leung, and M.-C. Chu, Phys. Rev. E **62**, 6584 (2000).
[37] G. Bekefi, *Radiation Processes in Plasmas* (Wiley, New York, 1966).
[38] D. J. Landau and E. M. Lifshitz, *Electrodynamics of Continuous Media* (Pergamon, Oxford, 1960).
[39] Y. B. Zel'dovich and Y. P. Raizer, *Physics of Shock Waves and High-Temperature Hydrodynamic Phenomena*, Vols. I and II (Academic Press, New York, 1966).
[40] D. A. Varshalovich, A. N. Moskalev, and V. K. Khersonskii, *Quantum Theory of Angular Momentum: Irreducible Tensors, Spherical Harmonics, Vector Coupling Coefficients, 3nj Symbols* (World Scientific, Singapore, 1988).
[41] J. D. Jackson, *Classical Electrodynamics*, 3rd ed. (Wiley, New York, 1999).
[42] S. C. Brown, *Basic Data of Plasma Physics* (MIT Press and Wiley, New York, 1959).
[43] M. A. Heald and C. B. Wharton, *Plasma Diagnostics with Microwaves* (Wiley, New York, 1965).
[44] P. J. Brussaard and H. C. V. D. Hulst, Rev. Mod. Phys. **34**, 507 (1962).
[45] S. Nozawa, N. Itoh, and Y. Kohyama, Astrophys. J. **507**, 530 (1998).
[46] N. Itoh, S. Kusano, T. Sakamoto, S. Nozawa, and Y. Kohyama, Astrophys. J., Suppl. Ser. **128**, 125 (2000).
[47] V. Fortov and I. Iakubov, *The Physics of Non-Ideal Plasma* (World Scientific, Singapore, 2000).
[48] V. Kamath and A. Prosperetti, J. Acoust. Soc. Am. **85**, 1538 (1987).
[49] A. Prosperetti and A. Lezzi, J. Fluid Mech. **168**, 457 (1986).
[50] N. Xu, L. Wang, and X. Hu, Phys. Rev. Lett. **83**, 2441 (1999).
[51] A. Prosperetti, J. Acoust. Soc. Am. **61**, 17 (1977).
[52] S. Hilgenfeldt, D. Lohse, and W. C. Moss, Phys. Rev. Lett. **80**, 1332 (1998).
[53] R. Pecha, B. Gompf, G. Nick, Z. Q. Wang, and W. Eisenmenger, Phys. Rev. Lett. **81**, 717 (1998).